

Robust Deep Compressive Sensing with Recurrent-Residual Structural Constraints

Jun Niu

Abstract—Existing deep compressive sensing (CS) methods either ignore adaptive online optimization or depend on costly iterative optimizer during reconstruction. This work explores a novel image CS framework with recurrent-residual structural constraint, termed as R²CS-NET. The R²CS-NET first progressively optimizes the acquired samplings through a novel recurrent neural network. The cascaded residual convolutional network then fully reconstructs the image from optimized latent representation. As the first deep CS framework efficiently bridging adaptive online optimization, the R²CS-NET integrates the robustness of online optimization with the efficiency and nonlinear capacity of deep learning methods. Signal correlation has been addressed through the network architecture. The adaptive sensing nature further makes it an ideal candidate for color image CS via leveraging channel correlation. Numerical experiments verify the proposed recurrent latent optimization design not only fulfills the adaptation motivation, but also outperforms classic long short-term memory (LSTM) architecture in the same scenario. The overall framework demonstrates hardware implementation feasibility, with leading robustness and generalization capability among existing deep CS benchmarks.

Index Terms—Compressive sensing, structural constraint, adaptive online optimization, recurrent neural network.

I. INTRODUCTION

Information compression and reconstruction stands at the center of communication and signal processing. Compressive sensing (CS) has been an emerging strategy to recover original signals with considerably fewer measurements at sub-Nyquist sampling rate [1], [2]. Different from auto-encoders, where both encoder and decoder can be heavily engineered, conventional CS seeks to alleviate the sampling complexity while reconstructing signals from low-dimensional measurements via computationally intensive optimization. Its sampling efficiency accommodates limited sensor-side computational resources and transmission bandwidth. Compared with deploying complex encoder at the frontend, CS serves as a more economic and realistic option. The online optimization further offers extra robustness to amend measurement noise during reconstruction. Benefiting from its flexible and efficient architecture, CS has been successfully applied in scenarios where measurements are expensive and noisy. Typical applications include magnetic resonance imaging (MRI) and high resolution imaging systems [3], [4].

Classic CS theory assumes the signal to be sparse or can be expressed as a sparse linear combination of known basis. This strong requirement hinders CS's practical application as such basis is implicit in general. Recently, Bora et al. introduces

deep learning based structural constraint to relax this requirement [5]. A *pre-trained* deep neural network (NN) is proposed as the structural constraint in the place of sparsity, which suffices a generalized set-restricted eigenvalue condition. With deep structural constraint and successful training, low reconstruction error for dense signals can still be achieved with high probability. The reconstruction, however, heavily relies on classic iterative optimization. Its slow convergence remains a critical challenge in practice. In addition, the sampling relies on random measurement matrices, which is sub-optimal for highly structured signals such as natural images.

Inspired by deep NN's powerful ability in signal representation, several deep CS methods are proposed to enhance the performance of both sampling and reconstruction. For example, Wu S. et al. [6] proposed an unrolled feed-forward NN for learning the measurement matrix, while depending on classic iterative optimization for reconstruction. Kulkarni et al. proposed a non-iterative deep reconstruction model, the ReconNet [7]. It achieves high efficiency and robustness with convolutional neural network (CNN), though the architecture does not emphasize domain insights. The DR²-NET [8] applies residual learning for reconstruction enhancement. The MS-DCI [9] develops an elegant multi-scale sampling framework with cascaded multi-stage reconstruction. The multi-level sampling decomposition, however, potentially increases the sampling hardware complexity or transmission bandwidth. More recent frameworks, such as OPINE-NET [10] and AMP-NET [11], unfold iterative optimization algorithms for model based methods into networks. Though efficient and interpretable, the unrolled networks possess reduced robustness and generalization capacity versus the iterative online optimizers. As an alternative, recently Wu Y. et al. [4] combines explicit online optimization with learnable deep structural constraint and measurement matrix. This framework largely speeds up the convergence of online optimization. However, it still relies on the classic iterative gradient descent optimizer for adaptive optimization, which is computationally costly and slow.

This work proposes a novel framework, termed as R²CS-NET, to effectively bridge deep image CS with adaptive online optimization. In particular, a novel recurrent neural network (RNN) is explored as an alternative for unrolled NN during initial reconstruction. It aims to enhance the structural constraint's capacity, such that the overall system operates more robustly and better generalizes in online usage, while avoiding expensive operations like iterative gradient calculation. The R²CS-NET is composed of three stages: measurement, recurrent latent optimization, and residual convolutional reconstruction. The measurement stage assembles a learnable, modified structural random matrix [12]. It is the only module deployed

This is a pre-print.

Jun Niu is now with Amazon (e-mail: j.niu1990@gmail.com). This work is done at Department of Electrical and Computer Engineering, Duke University, Durham, North Carolina, 27708, USA, before him joining Amazon.

at the sensor frontend, and exploits switchable pre-coded masks to adapt the R²CS-NET in different sampling domains without re-train necessity. The recurrent latent optimization attempts to acquire the robustness and generalization capacity of online optimization. This stage is established through a novel recurrent pipeline. It progressively optimizes the latent representation of the acquired samplings to accommodate the downstream reconstruction network. The residual CNN then fully reconstructs the original image in pixel domain. The recurrent latent optimization network and cascaded residual CNN together serve as the structural constraint in the place of sparsity. All components are fully convolutional for concurrency acceleration. The three stages are optimized jointly during training toward optimal reconstruction quality under given sampling rate.

Signal correlations have been addressed through the network architecture. The adaptive sensing nature of R²CS-NET further makes it an ideal candidate for color image CS. Numerical experiments verify the efficiency and robustness of the proposed design. The R²CS-NET also demonstrates leading performance among recent deep CS benchmarks.

In summary, this work contributes the following.

- The R²CS-NET is the first deep CS framework bridges efficient online optimization with unrolled reconstruction network. Expensive operations such as gradient computations are completely avoided during reconstruction.
- A novel recurrent-residual architecture is explored to enhance the generalization capacity and robustness of deep structural constraints.
- The R²CS-NET intrinsically supports color image CS. The overall system exhibits leading performance among deep CS benchmarks.

II. DEEP COMPRESSIVE SENSING WITH STRUCTURAL CONSTRAINTS AND ONLINE OPTIMIZATION

Compressive sensing aims to efficiently acquire a compressible signal \mathbf{x} and then reconstruct the original signal from samplings \mathbf{m} via finding optimal solutions to the under-determined linear equation system. Exploiting signal's sparsity or incoherence nature, the original signal can be recovered with far fewer samplings required by the Nyquist–Shannon sampling theorem. Formally,

$$\mathbf{m} = \mathbf{F}\mathbf{x} + \boldsymbol{\eta}, \quad (1)$$

where \mathbf{F} is the measurement matrix and $\boldsymbol{\eta}$ denotes the noise at measurement time. Depending on the sparsity of original signal \mathbf{x} , the dimension of measured signal \mathbf{m} is usually considerably smaller than that of \mathbf{x} .

A necessary and sufficient condition for this problem to be well conditioned is the Restricted Isometry Property (RIP). It states, for a small constant $\delta \in (0, 1)$, the difference between two signals $\mathbf{x}_1 - \mathbf{x}_2$ satisfies

$$\begin{aligned} (1 - \delta)\|\mathbf{x}_1 - \mathbf{x}_2\|^2 &\leq \|\mathbf{F}(\mathbf{x}_1 - \mathbf{x}_2)\|_2^2 \\ &\leq (1 + \delta)\|\mathbf{x}_1 - \mathbf{x}_2\|_2^2. \end{aligned} \quad (2)$$

In other words, the measurement matrix \mathbf{F} preserves the distance between original sparse signals with small perturbation

[4]. The original signal thus can be recovered by solving the optimization problem

$$\hat{\mathbf{x}} = \arg \min_{\mathbf{x}} \|\mathbf{m} - \mathbf{F}\mathbf{x}\|_2^2. \quad (3)$$

Classic CS theory requires \mathbf{x} to be a sparse signal or a dense signal that can be expressed as a sparse linear combination of known basis vectors. This enforces a strong restriction. In most practical problems the sparse basis vectors are not explicit to discover, sometimes extremely untrivial to obtain.

As an alternative, Bora et al. [5] propose using a *pre-trained* deep NN as the structural constraint in the place of sparsity

$$\mathbf{x} = G(\mathbf{z}). \quad (4)$$

The network $G(\cdot)$ implicitly constrains the compressibility through its architecture, where the latent space tensor \mathbf{z} 's dimension is usually considerably smaller than that of \mathbf{x} . This condition is sufficient to provide a generalized Set-Restricted Eigenvalue Condition (S-REC). It guarantees that low reconstruction error can be achieved with high probability.

Instead of directly solving Eq. (3), the reconstruction now first estimates the latent representation \mathbf{z} by solving the online optimization problem

$$\hat{\mathbf{z}} = \arg \min_{\mathbf{z}} \|\mathbf{m} - \mathbf{F}G(\mathbf{z})\|_2^2, \quad (5)$$

then reconstructs the original signal through $\hat{\mathbf{x}} = G(\hat{\mathbf{z}})$.

The structural constrained CS framework connects deep learning with classic CS theory. It provides a theoretical foundation to tackle arbitrary dense, compressible signals in data-driven manner. A few deep CS methods have been proposed thereafter. For example, the reconstruction can be accomplished through either classic optimizers or unrolled NN designs; the structural constraint G can be learnt together with the measurement matrix to achieve better reconstruction quality [4], [10], [13]–[15]. However, whenever adaptive online optimization is leveraged during the reconstruction, the gradient-based optimization of Eq. (5) has to be addressed in every iteration. As the structural constraint typically consists of heavy-weight NN, repeated evaluation of $\frac{\partial G(\mathbf{z})}{\partial \mathbf{z}}$ along the iterative optimization turns out to be extremely expensive. The computational cost further increases with more complex architecture designs. The unrolled NN reconstruction sidesteps the cost concerns. However, ignoring the adaptive online optimization potentially leads to sub-optimal solution with non-perfect $G(\cdot)$, impairing the system's robustness under the inevitable measurement noise in practice. An efficient, robust deep CS solution remains at the center of the problem.

III. R²CS-NET: A NOVEL IMAGE COMPRESSIVE SENSING FRAMEWORK

This work introduces a novel framework to efficiently bridge deep CS with adaptive online optimization. The proposed R²CS-NET consists of three main stages: measurement, recurrent latent optimization, and residual convolutional reconstruction. The measurement stage is engineered with simplicity and hardware implementation feasibility. With acquired samplings, an RNN first progressively adapts the samplings' latent

representation to the downstream reconstruction network. The residual CNN then fully reconstructs the original image. The recurrent latent optimization and the residual CNN together serve as the recurrent-residual structural constraint. It delivers higher generalization capacity and robustness than unrolled networks at moderate latency.

Each stage has its specific motivation. However, the three objectives are not mutually independent. All stages can be cascaded into an end-to-end system during training. A system sketch is illustrated in Fig. 1. The network architecture exploits signal correlation for optimal sampling efficiency.

IV. MEASUREMENT

The measurement stage is the only module deployed with sensors. One primary difference between CS and auto-encoders is the emphasis on efficiency and simplicity of data acquisition. The measurement stage is therefore engineered with hardware compatibility in mind. It consists of two fully convolutional layers, one with switchable pre-coded kernels adapting the R²CS-NET from various data acquisition spaces to the preferred sampling space; the other operating as the standard measurement matrix. The measurement matrix is the only component to be learnt from data.

The first layer's operation can be written as

$$\mathcal{Y}^{[1]} = \mathbf{W}_M^{[1],mask} * \mathcal{X}, \quad (6)$$

where $*$ denotes the 2D convolution operator; \mathcal{X} is the image in acquisition domain; $\mathbf{W}_M^{[1],mask}$ is the adaptive coded mask. Convolution stride is chosen as $[N_1, N_2]$ along width and height dimension, respectively; N_1 and N_2 denotes the width and height of each sampling block. This layer has no trainable parameters. The parallelism nature of convolution operations further guarantees concurrency efficiency. Figure 2 depicts the mapping mechanism.

Without loss of generality, we consider pixel domain sampling as the default setting. The front layer maps pixel value into k-space to exploit natural images' spectral domain sparsity. Inspired by this operation's discrete cosine transform (DCT) nature, the following set of coded masks are plugged in place of convolutional kernels.

$$\begin{aligned} \mathbf{W}_{i,j,k,k+k_1 \cdot N_{ch}+k_2 \cdot N_1 N_{ch}}^{DCT} &= \sqrt{\frac{2}{N_1}} \sqrt{\frac{2}{N_2}} \alpha(k_1) \alpha(k_2) \cdot \\ &\cos\left[\frac{(2n_1+1)\pi k_1}{2N_1}\right] \cos\left[\frac{(2n_2+1)\pi k_2}{2N_2}\right], \quad (7) \\ i &= 0, 1, \dots, N_1 - 1, j = 0, 1, \dots, N_2 - 1, \\ k &= 0, \dots, N_{ch} - 1, \end{aligned}$$

where N_{ch} denotes the colorspace channel. The measurement then multi-scales on frequency bands of input images. This step largely relieves the complexity expectation of the followed operation, which now can solely focus on linear measurement without further domain transformation. When directly acquiring data in k-space, one can simply replace the above with a set of binary coded masks [16]. The entire R²CS-NET thereafter operates in the new sampling space without re-train necessity. Other acquisition spaces can be adapted accordingly.

The second convolutional layer samples the original image block by block, across image's channels

$$\mathcal{M} = \mathbf{W}_M^{[2]} * \mathcal{Y}^{[1]}, \quad (8)$$

where $\mathbf{W}_M^{[2]}$ is the learnable CS measurement matrix; \mathcal{M} is the tensor of measured samplings. The convolution kernel is set to be of size $[1, 1]$ with stride 1 for block-wise measurement. Each tensor slice in \mathcal{M} with unit width and unit height thus represents the measurements in one sampling block.

One observation is the above two layers assemble a modified, learnable structural random matrix (SRM) [12]. The SRM is defined as a product of matrices $\Phi = \mathbf{DTR}$, where \mathbf{D} is the subsampling matrix; \mathbf{T} is the transform kernel; \mathbf{R} is a randomizer. $\mathbf{W}_M^{[2]}$ and $\mathbf{W}_M^{[1],mask}$ perform in the place of \mathbf{D} and \mathbf{T} , respectively.

The measurement stage can be feasibly integrated on hardware with coded aperture cameras [17] or CS-CMOS cameras [18]. For example, the switchable coded mask $\mathbf{W}_M^{[1],mask}$ and the learnt measurement matrix $\mathbf{W}_M^{[2]}$ can be implemented as high resolution coded apertures modulating the optical field from the scene, with a low resolution focal plane aperture instated for sampling data acquisition. Only the coded aperture needs to be switched when operating pre-trained R²CS-NET in new sampling space. The computationally inexpensive coded mask and measurement matrix can also be realized in digital domain as on CS-CMOS cameras, whose on-chip processor is strictly restricted by limited power and area on sensors.

V. RECURRENT-RESIDUAL STRUCTURAL CONSTRAINT

The recurrent-residual structural constraint aims to bridge the advantages of adaptive online optimization with deep CS, while avoiding the intensive costs of classic iterative optimizers. A two-phase layout is proposed to this end. The recurrent latent optimization stage resembles the gradient descent optimization through a novel RNN architecture. It preliminarily updates the samplings in latent space. The cascaded residual CNN fully reconstructs the image thereafter. Compared with the unrolled NN methods, the recurrent-residual structural constraint better generalizes on input patterns. Though not citing particular noise prior, it expands the robustness under measurement noise through architecture design with successful data-driven training.

A. Recurrent Latent Representation Optimization

The latent representation can be generally of arbitrary shape. Aiming at preliminarily reconstructing toward the original image, here \mathbf{z} is designed with the same dimension as $\mathcal{Y}^{[1]}$. The gradient descent latent optimization is thus formulated as

$$\hat{\mathbf{z}}_{i+1} = \hat{\mathbf{z}}_i - \alpha \frac{\partial}{\partial \hat{\mathbf{z}}_i} \|F(\hat{\mathbf{z}}_i) - \mathcal{M}\|_2^2, \quad (9)$$

where the subscript i denotes the iteration step; $\hat{\mathbf{z}}_{i+1}$ is progressively updated through the incremental adjustment to $\hat{\mathbf{z}}_i$.

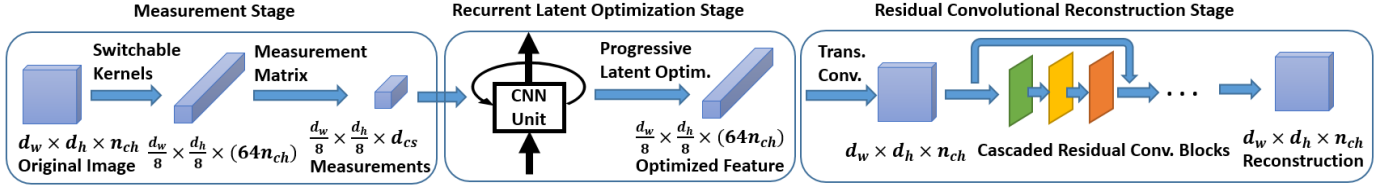


Fig. 1: Systematic sketch of the R^2CS -NET. The system consists of three stages: measurement, adaptive recurrent optimization, and residual convolutional reconstruction. Only the measurement stage needs to be deployed with frontend sensor hardware.

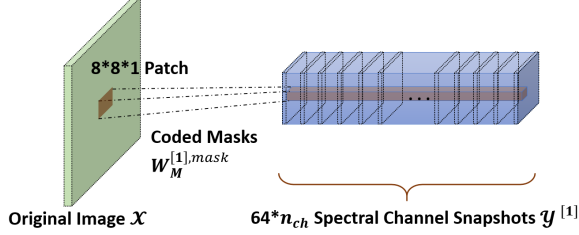


Fig. 2: Mapping input images from acquisition domain to k-space. The $W_M^{[1],mask}$ kernel is a set of $64 \times n_{ch}$ coded masks.

Our key observation is the stochastic gradient descent update of Eq. (9) resembles the cell state update in classic RNNs [19],

$$\mathcal{C}_t = f_t \odot \mathcal{C}_{t-1} + i_t \odot \tilde{\mathcal{C}}_t, \quad (10)$$

where the subscript t denotes the recurrent step; $-i_t$ operates as the learning rate and the new candidate state $\tilde{\mathcal{C}}_t$ corresponds to the incremental adjustment; f_t operates as the reset coefficient for the previous state; \odot denotes the Hadamard product.

This encourages us to design a recurrent unit assembling similar online latent optimization. Each iteration in Eq. (9) explicitly depends on the previous output $\hat{\mathcal{Z}}_i$ and the original measurements \mathcal{M} . This is robust in clean sampling environment. However, with the presence of measurement noise, the optimization deviates from the reconstruction goal due to the noisy \mathcal{M} . We consider a similar RNN. At each step, the recurrent unit consumes $\hat{\mathcal{Z}}_i$ and $F(\hat{\mathcal{Z}}_i) - \mathcal{M}$ as inputs. In noisy sampling environment both $F(\hat{\mathcal{Z}}_i)$ and \mathcal{M} are perturbed. Their absolute difference along the iterations converges towards a non-zero random variable. This residual potentially indicates environmental attributes such as noise variance, and assists the RNN amending the latent representation.

The second intuition is the wavelet decomposition nature of measurement residuals. The linear measurement operation maintains the residuals in the same space along the optimization steps. This is comparable to a wavelet sequence. One transform that successfully updates one packet is highly likely to successfully update the next packet in the same space.

A novel RNN is proposed based on the above analysis to progressively optimize the samplings' latent representation through measurement residuals. At each step, the recurrent unit operates upon the residual between the original samplings and measurements of previous step's output. The residual even-

tually converges to zero in noise-free environment. In noisy measurement environment, it highlights the noise attributes for further denoising amendment. This architecture together with successful data-driven training serves as the prior that enhances the system's noise robustness. One practical concern, however, is the measurement residuals vary in magnitudes over the recurrence. The recurrent unit is expected to possess consistent performance over wide bandwidth. To tackle this challenge, a scaling gate network renders the residual input with appropriate gain before generating the new candidate. i_t and f_t are both designed as CNNs to further enhance the recurrent unit's capacity.

Summarily, at the initial step, the input \mathcal{I}_0 is initialized with the measurement sampling \mathcal{M} . At each following step i , the recurrent unit updates the latent representation \mathcal{Z}_i as

$$\begin{aligned} \mathcal{I}_i &= S(F(\mathcal{Z}_{i-1}) - \mathcal{I}_0), \\ \mathcal{H}_i &= C(\mathcal{I}_i), \\ \mathcal{Z}_i &= R(\mathcal{Z}_{i-1}, \mathcal{H}_i) \odot \mathcal{Z}_{i-1} + U(\mathcal{Z}_{i-1}, \mathcal{H}_i) \odot \mathcal{H}_i, \\ i &= 1, 2, \dots, T. \end{aligned} \quad (11)$$

Here $S(\cdot), C(\cdot), R(\cdot), U(\cdot)$ are all CNNs instead of coefficients; $F(\cdot)$ is the measurement operation following Eq. (8). The scaling gate $S(\cdot)$ adjusts the residual input with appropriate gain at each step. The candidate gate $C(\cdot)$ generates a new candidate from scaled input. The latent representation is then updated as a trade-off between previous result and new candidate, where the reset gate $R(\cdot)$ and the update gate $U(\cdot)$ calculate the trade-off coefficients, respectively.

Conventional LSTM and GRU cells use dense connection architecture. This contradicts with the uncorrelated nature of samplings measured from different image blocks, simultaneously resulting in numerous unnecessary parameters. As an alternative, $S(\cdot), C(\cdot), R(\cdot), U(\cdot)$ consist of 2D convolution layers with kernel size $[1, 1]$ and stride 1. Operating on the latent representation sampling block by sampling block, it successfully avoids block-wise coupling. A batch normalization layer is further added at the recurrent input and output to enhance nonlinear processing capability.

Figure 3 - 4 depicts the proposed recurrent unit architecture and computation pipeline, respectively. At the initial step the candidate gate directly operates on the measured samplings \mathcal{M} . Latent representation then receives progressive updates from previous step's output and measurement residual. All network parameters are shared across the recurrent steps.

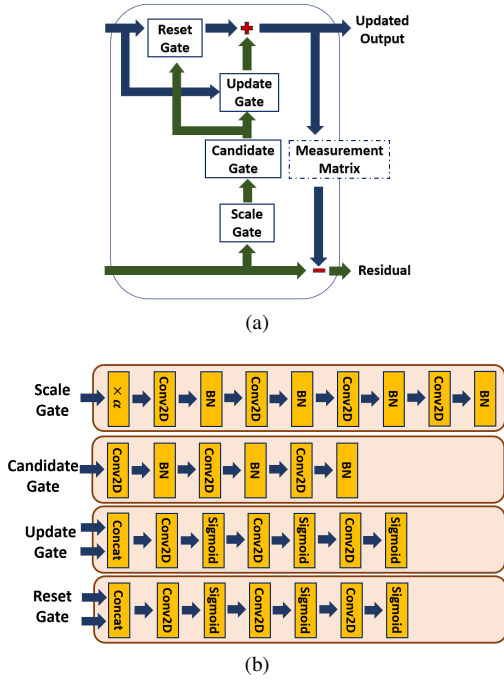


Fig. 3: Recurrent unit architectures for latent optimization: (a) the overall sketch; (b) network designs for each inner gate.

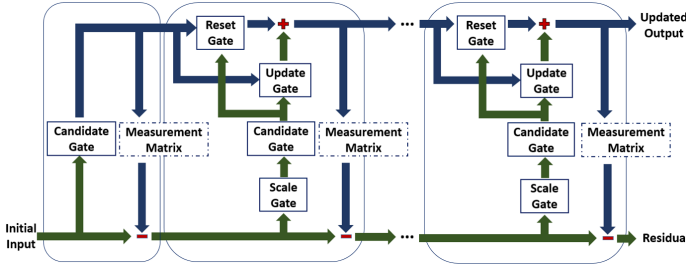


Fig. 4: Computational pipeline for recurrent latent optimization. The initial step evaluates on the measurement samplings. The following steps first scale the residual input and then update latent representation with trade-off.

B. Residual Convolutional Reconstruction

This stage reconstructs the original image from the optimized latent representation \mathcal{Z} . Formally, the residual CNN $G(\cdot)$ aims to reconstruct an image $\hat{\mathcal{X}} = G(\mathcal{Z})$ such that $\hat{\mathcal{X}}$ is as close to the original image \mathcal{X} as possible. Sharpness enhancement and artifacts suppression need to be accomplished toward this goal.

Successful reconstruction relies on comprehending the intrinsic correlation of \mathcal{Z} 's components. Here we first enrich the latent representation through cascaded convolutions

$$G^{[l]}(\mathcal{Z}) = BN(\mathbf{W}_G^{[l]} * G^{[l-1]}(\mathcal{Z}) + \mathbf{B}_G^{[l]}), l = 1, 2 \quad (12)$$

where $BN(\cdot)$ denotes a batch normalization layer; superscript $[l]$ denotes the layer index. $\mathbf{W}_G^{[1]}$ and $\mathbf{W}_G^{[2]}$ contain $N_1 \times N_2 \times N_{ch}$ channels. The block-wise latent optimization addresses the inter-channel correlation while maintaining the

relative independency across adjacent sampling blocks. As a result, both kernels are correspondingly designed as size $[1, 1]$ with stride 1.

A transposed convolution layer then maps $G^{[2]}(\mathcal{Z})$ to the original image's shape

$$\tilde{G}^{[3]}(\mathcal{H}) = \mathbf{C}_G^{[3]T} \cdot \tilde{G}^{[2]}(\mathcal{Z}) + \mathbf{B}_G^{[3]}, \quad (13)$$

where \cdot denotes the matrix multiplication; $\mathbf{C}_G^{[3]}$ is the matrix operator of the transposed convolution; $\tilde{G}^{[2]}(\cdot)$ and $\tilde{G}^{[3]}(\cdot)$ denote the row-major order vector representation of the tensor outputs of $G^{[2]}(\cdot)$ and $G^{[3]}(\cdot)$, respectively. After this operation, the latent representation is transformed to be in same shape as \mathcal{X} , while maintaining the same number of entries.

The initial macroblocking artifacts suppression is achieved with three cascading convolution layers with the same operations described by Eq. (12). The transposed convolution maps entries along tensor channels to width and height dimensions. As a result, the convolution kernels of shape $[11, 11]$, $[7, 7]$ and $[1, 1]$ are used to exploit the intra-channel spatial correlation of $G^{[3]}(\mathcal{Z})$. To guarantee the initial decoding results falling into the non-negative pixel value range, a rectifier linear unit (ReLU) function activates the output of $G^{[6]}$.

With macroblocking artifacts mitigated, detail enhancement remains the next objective towards high quality reconstruction. Here we apply cascaded residual CNNs for image sharpening. Operations in each residual block can be formulated as

$$G^{[l]}(\mathcal{H}) = \begin{cases} \mathbf{W}_G^{[l]} * G^{[l-1]}(\mathcal{H}) + \mathbf{B}_G^{[l]} + G^{[l-3]}(\mathcal{H}), & l = 9, 12, 15, 18, 21 \\ ReLU(BN(\mathbf{W}_G^{[l]} * G^{[l-1]}(\mathcal{H}) + \mathbf{B}_G^{[l]})), & l = 7, 8, \dots, 20. \end{cases} \quad (14)$$

This architecture conceptually decomposes the image into wavelet series. The convolution layers inside each residual block focuses on sharpening high frequency details. After merging with the low frequency image snapshots, features of the complete image are delivered to the next cascaded residual block for further enhancement.

Passing through five cascaded residual convolution blocks, the final reconstruction is activated with a ReLU function:

$$\hat{\mathcal{X}} = ReLU(G^{[21]}(\mathcal{H})). \quad (15)$$

It enforces pixel values into the non-negative definition range, and enhances the model's nonlinear capacity in the meantime.

VI. LEARNING MEASUREMENT MATRIX AND STRUCTURAL CONSTRAINT

Successful learning fulfills each of the R²CS-NET's three stages its particular role. An effective measurement stage enforces the RIP condition while collaborating with the reconstruction stages for optimal sampling efficiency. This objective can be described through the measurement loss [4]

$$L_M = \frac{1}{N} \sum_{i=1}^N (\|F(\hat{\mathcal{X}}_i - \mathcal{X}_i)\|_2^2 - \|\hat{\mathcal{X}}_i - \mathcal{X}_i\|_2^2)^2, \quad (16)$$

where N is the number of training images.

Meanwhile, the recurrent latent optimization stage adapts the samplings to accommodate the downstream reconstruction. Given a *trained* downstream network, this objective is outlined by the loss function

$$L_R = \frac{1}{N} \sum_{i=1}^N \|F \cdot G(\hat{\mathbf{Z}}_i) - F(\mathbf{x}_i)\|_2^2, \quad (17)$$

where $\hat{\mathbf{Z}}_i$ denotes the optimized latent representation of samplings; $G(\hat{\mathbf{Z}}_i)$ reconstructs \mathbf{x}_i .

The residual convolutional stage minimizes the discrepancy between final reconstructions and the ground truth. One common formulation is the mean squared error (MSE) loss

$$L_{MSE} = \frac{1}{N} \sum_{i=1}^N \|\hat{\mathbf{x}}_i - \mathbf{x}_i\|_2^2. \quad (18)$$

It equivalently optimizes the reconstructed images' peak signal-to-noise ratio (PSNR) [16], [20]. However, according to specific engineering applications, the loss function can be easily revised to address other perceptual quality metrics [21].

Each stage can be trained separately toward its goal or iteratively updated in interaction. However, despite the distinct motivations, the three objectives are not mutually independent. L_R and L_M simultaneously reach their minimum with optimized discrepancy between final reconstruction $\hat{\mathbf{x}}$ and the ground truth \mathbf{x} . Cascading as an end-to-end system during training, all stages can be jointly trained under L_{MSE} . This is applied as a preferred training strategy realizing it not only avoids potential slow convergence, but also enforces the optimal sampling - reconstruction of the overall system.

VII. EXPERIMENTS

This section provides intensive experiments to validate the efficiency and performance of the proposed R²CS-NET framework. Without loss of generality, we set the recurrent optimization length as $T = 20$ and sampling block size as $8 \times 8 \times N_{ch}$. These hyper-parameters are empirically selected with accommodating the limited computational resources. Though not optimized through intensive hyper-parameter search, the R²CS-NET shows leading performance among existing deep CS benchmarks. The advantage of the proposed recurrent-residual constraint is demonstrated through its enhancement to reconstruction quality and noise robustness under various measurement noise levels. Comparison with classic online optimization methods demonstrates the R²CS-NET achieves comparable sensing fidelity at considerably higher efficiency.

A. Training

The training and validation datasets are cropped from the DIV2K dataset [22], which consists of 1,000 high quality color images of 2K resolution. Without loss of generality, we set the dimension of training images as $128 \times 128 \times 3$, where the last dimension denotes the images' RGB channels in pixel domain. The R²CS-NET framework, however, is insensitive to the image size. The entire training dataset contains 1,098,400 images at 128×128 resolution and the validation dataset has 1000

images at the same resolution. The training, validation and testing datasets throughout the discussion share no overlap.

Assembled as an end-to-end system, all modules are updated interactively by minimizing Eq. (18) with Adam optimizer. The recurrent-residual structural constraint enhances the generalization capacity in architecture. This potential needs to be further attained through appropriate data-driven training. An environmental noise is thus engineered to instill the robustness under practical application. Throughout the training process, a white Gaussian noise with standard deviation $\sigma = 0.1$ is added to all measurement operations during sampling and recurrent latent optimization. This perturbation is empirically chosen to the extent that no noticeable reconstruction deterioration is observed in noise-free environment. Once training completes, the R²CS-NET can reconstruct images at arbitrary resolution and operate under arbitrary noise level.

B. Validating the Recurrent Latent Optimization

We first validate the recurrent latent optimization design with ablation study. Sampling and reconstructing the *Lena* image in Set14, Fig. 5 illustrates the samplings' latent representation at various recurrent steps. The latent features are progressively optimized to accommodate the downstream reconstruction. Evolvement and convergence can be easily observed along the snapshots. Figure 6 demonstrates the reconstructed image at each optimization step, evaluated under PSNR and structural similarity index measure (SSIM) metrics. The quality evolvement aligns with the progressive optimization principle and successfully verifies the architecture design.

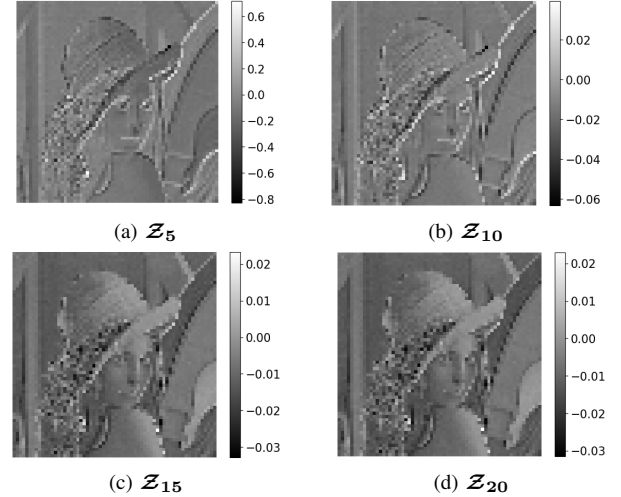


Fig. 5: Optimized latent representation \mathbf{Z}_i at recurrent step $i = 5, 10, 15, 20$, illustrating the tensor's first channel.

C. Sampling Efficiency and Reconstruction Quality

The efficiency of learnable measurement matrix, the effectiveness of the residual CNN reconstruction, and the contribution of recurrent latent optimization are further validated through lateral comparison with control group counterparts.

TABLE I: Model Performance on LIVE1, Set5, Set14, BSD300, BSD500 Datasets*: Using Averaged PSNR (dB) and SSIM Metrics (1st & 2nd Column under each Dataset), and Time Cost (s) to Sample and Reconstruct All Images in LIVE1.+

Sampling Rate	Model	Dataset							Time Cost on LIVE1	Trainable Parameters			
		LIVE1	Set5	Set14	BSD300	BSD500							
0.02	Random-RCS	22.48	0.748	23.95	0.813	22.35	0.743	23.20	0.740	23.02	0.756	8.92	605,203
	RCS	24.40	0.794	26.85	0.874	24.65	0.802	25.13	0.787	25.02	0.803	7.56	605,375
	RCS-GD-20	24.46	0.796	26.98	0.876	24.74	0.804	25.21	0.789	25.09	0.805	206.82	605,375
	RCS-GD-100	24.52	0.798	27.10	0.879	24.82	0.806	25.27	0.792	25.16	0.808	635.66	605,375
	R ² CS-LSTM	24.43	0.794	26.82	0.873	24.63	0.801	25.14	0.786	25.02	0.803	13.45	806,700
	R ² CS-NET	24.54	0.794	26.99	0.878	24.78	0.805	25.25	0.790	25.13	0.806	13.50	1,028,581
0.05	Random-RCS	25.34	0.833	27.52	0.891	25.29	0.829	25.74	0.821	25.75	0.838	8.16	605,965
	RCS	27.11	0.882	29.91	0.927	27.22	0.878	27.73	0.875	27.74	0.886	7.39	607,895
	RCS-GD-20	27.21	0.885	30.09	0.929	27.35	0.881	27.82	0.877	27.84	0.890	202.15	607,895
	RCS-GD-100	27.31	0.887	30.29	0.932	27.48	0.884	27.92	0.881	27.95	0.893	630.75	607,895
	R ² CS-LSTM	27.25	0.885	30.05	0.929	27.39	0.882	27.75	0.876	27.80	0.890	13.23	811,668
	R ² CS-NET	27.50	0.889	30.33	0.933	27.59	0.885	27.97	0.880	28.03	0.893	14.24	1,033,099
0.10	Random-RCS	27.43	0.892	29.74	0.924	27.16	0.880	27.83	0.884	27.92	0.896	8.87	607,108
	RCS	29.69	0.932	32.05	0.948	29.53	0.922	30.20	0.928	30.32	0.936	7.28	610,775
	RCS-GD-20	29.87	0.935	32.42	0.952	29.74	0.925	30.38	0.931	30.53	0.939	203.36	610,775
	RCS-GD-100	30.08	0.938	32.81	0.956	29.98	0.927	30.59	0.934	30.76	0.942	637.59	610,775
	R ² CS-LSTM	30.09	0.938	32.54	0.954	29.91	0.927	30.54	0.933	30.70	0.942	13.14	821,145
	R ² CS-NET	30.31	0.940	32.79	0.957	30.09	0.929	30.72	0.935	30.89	0.943	13.39	1,043,116
0.20	Random-RCS	30.66	0.946	32.45	0.951	29.69	0.922	31.25	0.946	31.32	0.950	8.81	609,648
	RCS	33.97	0.973	35.35	0.970	32.82	0.955	34.74	0.974	34.77	0.976	7.32	617,175
	RCS-GD-20	34.33	0.975	35.82	0.973	33.15	0.958	35.14	0.976	35.19	0.978	207.00	617,175
	RCS-GD-100	34.75	0.978	36.43	0.976	33.54	0.960	35.62	0.979	35.69	0.980	639.78	617,175
	R ² CS-LSTM	34.67	0.978	35.90	0.974	33.47	0.961	35.34	0.978	35.42	0.980	13.25	840,405
	R ² CS-NET	34.79	0.978	35.97	0.974	33.56	0.961	35.54	0.978	35.59	0.980	13.62	1,079,296
0.30	Random-RCS	33.46	0.971	34.92	0.966	31.92	0.944	34.36	0.972	34.37	0.974	8.83	612,061
	RCS	37.07	0.984	37.45	0.977	35.05	0.967	37.83	0.986	37.79	0.986	7.41	623,255
	RCS-GD-20	37.78	0.987	38.22	0.981	35.65	0.970	38.67	0.989	38.60	0.989	217.13	623,255
	RCS-GD-100	38.68	0.990	39.33	0.984	36.45	0.974	39.74	0.991	39.65	0.991	645.36	623,255
	R ² CS-LSTM	37.98	0.989	38.36	0.982	35.97	0.973	39.10	0.990	38.96	0.990	13.14	858,702
	R ² CS-NET	38.90	0.991	39.07	0.984	38.90	0.991	39.87	0.992	39.73	0.992	13.54	1,131,451

*LIVE1, Set5, Set14, and test sets of BSD300, BSD500 contain 29, 5, 14, 100, and 200 color images, respectively.

+The best and second best results are highlighted in **red** and **blue**, respectively. Their time costs are highlighted in **bold**.

Each of the following architectures is investigated on NVIDIA GeForce RTX 2080 Super GPU with the same runtime setting.

- Random-RCS: samples with fixed, classic random measurement matrix; reconstructs via the residual CNN without online optimization.
- RCS: samples with the learnable measurement matrix, with remaining parts the same as the Random-RCS.
- RCS-GD: employs the gradient descent adaptive online optimization upon the RCS, following Eq. (5). Iteration steps of 20 and 100 are investigated in the experiment, where convergence is empirically reached at 100 steps.
- R²CS-LSTM: employs the classic LSTM architecture for recurrent latent optimization upon the RCS. The LSTM unit passes measurement residuals in the same manner as the proposed recurrent-residual stage.
- R²CS-NET: the proposed framework.

Five groups of model instances are trained at 0.02, 0.05, 0.1, 0.2 and 0.3 sampling rate, respectively. Their statistical performance is evaluated on five widely used benchmark datasets: LIVE1 [23], Set5 [22], Set14 [22], and the test sets of BSD300 [24], BSD500 [25].

Table I summarizes the performance of each experimental group. The Random-RCS serves as the base case. Its samplings are acquired through random measurement matrix with no online optimization. The successful reconstruction, meanwhile, demonstrates the fundamental validity of the residual convolutional reconstruction stage. Comparison between the Random-

RCS and the RCS reveals the sampling efficiency delivered by the learnable measurement matrix. The CS methods with online optimization, namely the RCS-GD, R²CS-LSTM, and R²CS-NET, demonstrate better performance in general. The consistently superior reconstruction of the RCS-GD over the RCS indicates the significance of online optimization. Despite the RCS-GD's leading CS fidelity, its classic gradient descent online optimizer is extremely slow. The R²CS-NET employs the proposed recurrent latent optimization stage to achieve comparable reconstruction quality with considerably higher efficiency. Its time efficiency and slightly better fidelity over the RCS-GD-100 attest the effectiveness. As a control group, the R²CS-LSTM utilizes the classic convolutional LSTM unit for adaptive optimization. The proposed recurrent architecture in the R²CS-NET outperforms the LSTM in the same scenario. Though the R²CS-NET contains more parameters, the two methods operate at comparable speed.

Figure 7 shows the reconstructions of four methods on *Barbara* in Set14, from both clean and noisy measurement environment. The R²CS-NET achieves comparable fidelity as the RCS-GD-100, prevailing the methods absenting online optimization. The recurrent-residual structural constraint introduces moderate latency in adaptive optimization. However, decoupled from sampling, it has no direct impact on measurement latency or sensor hardware complexity.



Fig. 6: Reconstruction at various recurrent latent optimization steps. The R^2CS -NET operates at 0.1 sampling rate and is trained with default recurrent steps = 20.

D. Robustness under Measurement Noise

The recurrent latent optimization conceptually inherits the robustness of online optimization. The potential is further realized through measurement perturbation during training. This experiment investigates the R^2CS -NET's robustness under various measurement noise levels.

To demonstrate the noise robustness contributed by the recurrent-residual structural constraint, we again compare the R^2CS -NET with the RCS, the RCS-GD-100, and the R^2CS -LSTM. Figure 8a compares the four architectures under measurement noise level from $\sigma = 0$ to $\sigma = 1.0$. The RCS-GD-100 unsurprisingly shows highest robustness. Its iterative online optimization amends the latent representation at the trade-off of computational cost. Meanwhile, the R^2CS -NET gains stronger noise robustness over the RCS and the R^2CS -LSTM. The margin expands along the rising measurement noise level. The proposed recurrent unit outperforms the LSTM regarding noise robustness as well.

Figure 8b provides the R^2CS -NET's measurement noise sensitivity versus the benchmarks reported by the DR^2 -NET [8] and the ReconNet [7]. Based on the available benchmark data, the models are compared at $\sigma = 0, 0.01, 0.05, 0.1, 0.25, 0.5$, with 0.1 sampling rate. Under all noise levels, the R^2CS -NET demonstrates considerably higher robustness. The margin expands in higher noise region. For example, the DR^2 -NET and the ReconNet's reconstruction quality drops by 61% at $\sigma = 0.5$ noise level. On the contrary, the R^2CS -NET is only impaired by 13%.

Comparison between the R^2CS -NET and the RCS reveals the recurrent latent optimization's direct contribution against noise. Fig. 9 visualizes the two methods' reconstructions on *Monarch*. Enhancements are observed at all noise levels.

TABLE II: Model Comparison on the Color BSD500 Test Set, Using Averaged PSNR (dB) and SSIM Metrics (1st & 2nd Column under each Sampling Rate).

Dataset	Model	Sampling Rate					
		0.1		0.25		0.3	
BSD500 Test Set	ReconNet [7]	26.85	0.784	30.51	0.897	31.49	0.917
	CSNet+ [29]	29.07	0.820	33.26	0.925	34.52	0.945
	LDIT [28]	24.94	0.704	29.10	0.852	30.23	0.880
	LDAMP [28]	26.61	0.692	28.35	0.830	29.89	0.872
	DPDNN [31]	24.37	0.686	28.87	0.849	29.98	0.876
	NN [30]	23.44	0.644	26.42	0.776	27.23	0.804
	ISTA-NET+ [32]	25.46	0.502	29.92	0.738	32.21	0.769
	AMP-NET [11]	28.11	0.810	32.55	0.923	33.82	0.941
	R^2CS -NET	30.89	0.943	37.56	0.987	39.73	0.992

E. Comparing with Deep CS Benchmarks

Verified the R^2CS -NET's validity via stage-by-stage lateral comparisons, this section further investigates the overall framework's performance amidst recent deep CS benchmarks. The R^2CS -NET enlists its efficacy through learnable sampling and efficient adaptive reconstruction. The correlations across and within image channels are carefully addressed at both measurement and reconstruction stages. Additionally assisted with recurrent latent optimization, the R^2CS -NET's adaptive sensing nature makes it a natural candidate for color image CS. Table II first compares it with existing benchmarks on BSD500. Noticing most existing CS benchmarks are reported on grayscale images, a set of R^2CS -NET instances are further trained with single channel images. Table III inspects the candidates on Set11 [14], containing 11 grayscale images. Among the benchmarks, TVAL3 [26], DAMP [27] are classic model-based CS methods. LDIT [28], LDAMP [28] are based on random measurement, while the remaining methods generally support learning measurement matrix through data. ReconNet [7] and CSNet+ [29] employ classic deep network architecture, while AMP-NET [11], LDIT, LDAMP, NN [30], DPDNN [31], ISTA-NET+ [32] unfold the iterative optimization into feed-forward networks. CSNet+, LDIT, LDAMP fully address color images' channel correlation. R^2CS -NET is the first method integrates adaptive online optimization with unrolled network.

The adaptive online optimization as well as the R^2CS -NET's overall architecture successfully handles sampling correlation, contributing toward outstanding performance in color image CS. The margin over benchmark methods expands along with the sampling rate. Leading performance can also be observed on grayscale test. Figure 10 visualizes reconstructions on *Parrots* image in Set11 at 0.1 sampling rate. All methods sample pixel domain images except the R^2CS -NET_k. As a validation of the framework's sampling adaptivity, the R^2CS -NET_k transplants the R^2CS -NET for k-space sampling by merely switching the measurement mask. It achieves the same outcome except for inevitable rounding errors.

VIII. CONCLUSIONS AND FUTURE WORK

This work proposes a novel deep CS framework, termed as R^2CS -NET. Inspired by iterative online optimizers, a recurrent-residual structural constraint is explored for image CS. As an alternative for unrolled NN, it possess improved robustness and generalization capacity while maintaining high

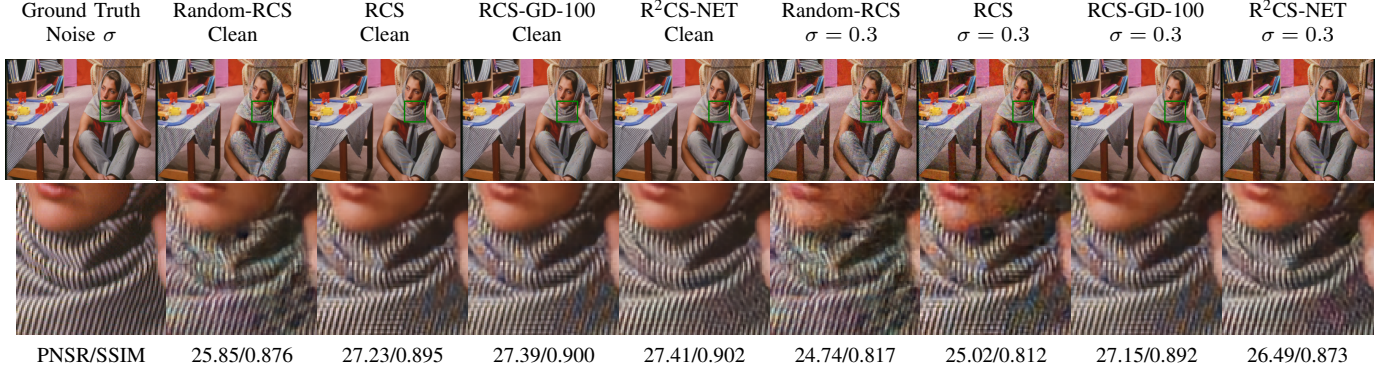
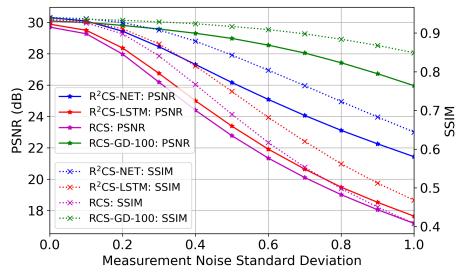
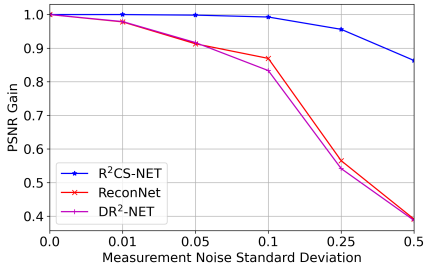


Fig. 7: Reconstructions on *Barbara* image in Set14 at sampling rate of 0.1. Highlighted regions are enlarged in the 2nd row.



(a) Reconstruction quality comparison across progressive latent optimization architectures.



(b) Measurement noise robustness comparison with reported benchmarks.

Fig. 8: Comparison between R²CS-NET and benchmarks under various measurement noise levels at 0.1 sampling rate.

efficiency. The R²CS-NET demonstrates leading CS quality and measurement noise robustness among existing benchmarks. Designs inspired by more advanced optimization models can be further investigated in specific application domains.

REFERENCES

- [1] R. G. Baraniuk, “Compressive sensing [lecture notes],” *IEEE Signal Processing Magazine*, vol. 24, no. 4, pp. 118–121, 2007.
- [2] E. J. Candes and M. B. Wakin, “An introduction to compressive sampling,” *IEEE Signal Processing Magazine*, vol. 25, no. 2, pp. 21–30, 2008.
- [3] J. C. Ye, “Compressed sensing mri: a review from signal processing perspective,” *BMC Biomedical Engineering*, vol. 1, no. 1, p. 8, Mar 2019.

TABLE III: Model Comparison on Grayscale Set11 Dataset, Using Averaged PSNR (dB) and SSIM Metrics (1st & 2nd Column under each Sampling Rate)

Dataset	Model	Sampling Rate					
		0.1		0.25		0.3	
Set11	DAMP [27]	19.87	0.376	31.62	0.723	32.64	0.754
	ReconNet [7]	27.63	0.849	32.07	0.925	33.17	0.938
	TVAL3 [26]	22.45	0.376	27.63	0.624	29.00	0.676
	CSNet+ [29]	27.76	0.851	32.76	0.932	33.90	0.945
	LDIT [28]	25.56	0.769	31.35	0.904	32.69	0.922
	LDAMP [28]	24.94	0.748	29.93	0.878	32.01	0.914
	DPDNN [31]	24.53	0.739	30.63	0.892	32.06	0.915
	NN [30]	22.99	0.659	26.57	0.784	27.64	0.810
	ISTA-NET+ [32]	25.93	0.784	32.27	0.917	33.66	0.933
	BCS-Net [14]	29.43	0.868	-	-	35.60	0.955
	AMP-NET [11]	29.45	0.879	34.59	0.948	35.90	0.957
	R ² CS-NET ^{1ch*}	29.88	0.936	34.29	0.974	35.14	0.978

* This is a set of single-channel models trained for grayscale image CS.

- [4] Y. Wu, M. Rosca, and T. Lillicrap, “Deep compressed sensing,” in *Proceedings of the 36th International Conference on Machine Learning*, ser. Proceedings of Machine Learning Research, K. Chaudhuri and R. Salakhutdinov, Eds., vol. 97. PMLR, 09–15 Jun 2019, pp. 6850–6860.
- [5] A. Bora, A. Jalal, E. Price, and A. G. Dimakis, “Compressed sensing using generative models,” in *Proceedings of the 34th International Conference on Machine Learning*, ser. Proceedings of Machine Learning Research, D. Precup and Y. W. Teh, Eds., vol. 70. PMLR, 06–11 Aug 2017, pp. 537–546.
- [6] S. Wu, A. Dimakis, S. Sanghavi, F. Yu, D. Holtmann-Rice, D. Storch, A. Rostamizadeh, and S. Kumar, “Learning a compressed sensing measurement matrix via gradient unrolling,” in *Proceedings of the 36th International Conference on Machine Learning*, ser. Proceedings of Machine Learning Research, K. Chaudhuri and R. Salakhutdinov, Eds., vol. 97. PMLR, 09–15 Jun 2019, pp. 6828–6839.
- [7] S. Lohit, K. Kulkarni, R. Kerviche, P. Turaga, and A. Ashok, “Convolutional neural networks for noniterative reconstruction of compressively sensed images,” *IEEE Transactions on Computational Imaging*, vol. 4, no. 3, pp. 326–340, 2018.
- [8] H. Yao, F. Dai, S. Zhang, Y. Zhang, Q. Tian, and C. Xu, “Dr2-net: Deep residual reconstruction network for image compressive sensing,” *Neurocomputing*, vol. 359, pp. 483–493, 2019.
- [9] T. N. Canh and B. Jeon, “Multi-scale deep compressive imaging,” *IEEE Transactions on Computational Imaging*, vol. 7, pp. 86–97, 2021.
- [10] J. Zhang, C. Zhao, and W. Gao, “Optimization-inspired compact deep compressive sensing,” *IEEE Journal of Selected Topics in Signal Processing*, vol. 14, no. 4, pp. 765–774, 2020.
- [11] Z. Zhang, Y. Liu, J. Liu, F. Wen, and C. Zhu, “Amp-net: Denoising-based deep unfolding for compressive image sensing,” *IEEE Transactions on Image Processing*, vol. 30, pp. 1487–1500, 2021.
- [12] T. T. Do, L. Gan, N. H. Nguyen, and T. D. Tran, “Fast and efficient com-

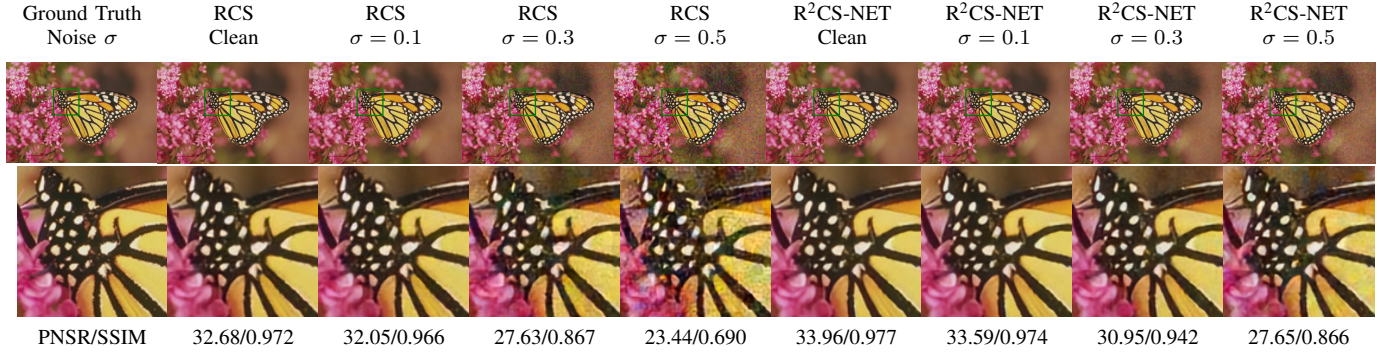


Fig. 9: R²CS-NET and RCS reconstruction on *Monarch* image in Set14 at sampling rate of 0.1, under various measurement noise levels. Highlighted regions are enlarged in the 2nd row.

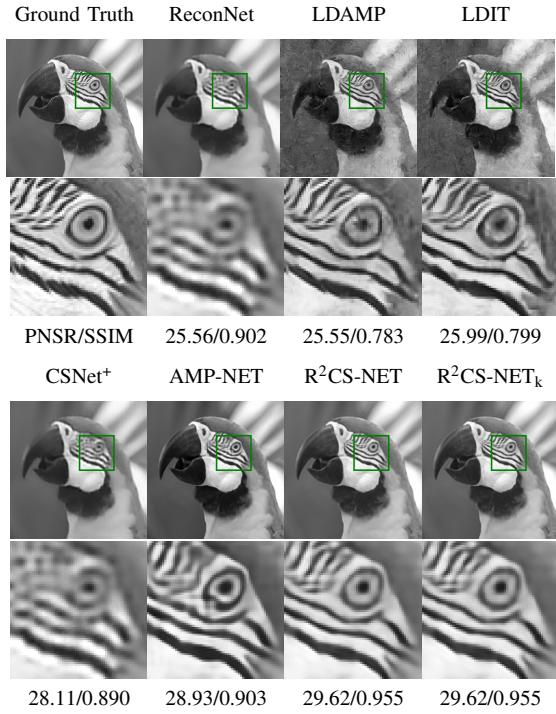


Fig. 10: Reconstructions on *Parrots* image in Set11 at 0.1 sampling rate. R²CS-NET_k acquires samplings in k-space; all others sample from pixel domain.

pressive sensing using structurally random matrices,” *IEEE Transactions on Signal Processing*, vol. 60, no. 1, pp. 139–154, 2012.

- [13] W. Shi, F. Jiang, S. Liu, and D. Zhao, “Scalable convolutional neural network for image compressed sensing,” in *Proceedings of the IEEE/CVF Conference on Computer Vision and Pattern Recognition (CVPR)*, June 2019.
- [14] S. Zhou, Y. He, Y. Liu, C. Li, and J. Zhang, “Multi-channel deep networks for block-based image compressive sensing,” *IEEE Transactions on Multimedia*, pp. 1–1, 2020.
- [15] W. Shi, F. Jiang, S. Liu, and D. Zhao, “Scalable convolutional neural network for image compressed sensing,” in *2019 IEEE/CVF Conference on Computer Vision and Pattern Recognition (CVPR)*, 2019, pp. 12 282–12 291.
- [16] J. Niu, “End-to-end jpeg decoding and artifacts suppression using heterogeneous residual convolutional neural network,” in *2020 International Joint Conference on Neural Networks (IJCNN)*, 2020, pp. 1–8.

- [17] A. Wagadarikar, R. John, R. Willett, and D. Brady, “Single disperser design for coded aperture snapshot spectral imaging,” *Appl. Opt.*, vol. 47, no. 10, pp. B44–B51, Apr 2008.
- [18] M. Zhang, Y. Wang, and A. Bermak, “Block-based compressive sampling for digital pixel sensor array,” in *2nd Asia Symposium on Quality Electronic Design (ASQED)*, 2010, pp. 9–12.
- [19] X. Shi, Z. Chen, H. Wang, D.-Y. Yeung, W.-k. Wong, and W.-c. Woo, “Convolutional lstm network: A machine learning approach for precipitation nowcasting,” in *Proceedings of the 28th International Conference on Neural Information Processing Systems - Volume 1*, ser. NIPS’15. Cambridge, MA, USA: MIT Press, 2015, p. 802–810.
- [20] C. Dong, C. C. Loy, K. He, and X. Tang, “Image super-resolution using deep convolutional networks,” *IEEE Transactions on Pattern Analysis and Machine Intelligence*, vol. 38, no. 2, pp. 295–307, Feb 2016.
- [21] J. M. Johnson, A. Alahi, and F.-F. Li, “Perceptual losses for real-time style transfer and super-resolution,” in *ECCV*, 2016.
- [22] R. Timofte, S. Gu, J. Wu, L. Van Gool, L. Zhang, M.-H. Yang, M. Haris *et al.*, “Ntire 2018 challenge on single image super-resolution: Methods and results,” in *The IEEE Conference on Computer Vision and Pattern Recognition (CVPR) Workshops*, June 2018.
- [23] H. R. Sheikh, M. F. Sabir, and A. C. Bovik, “A statistical evaluation of recent full reference image quality assessment algorithms,” *IEEE Transactions on Image Processing*, vol. 15, no. 11, pp. 3440–3451, Nov 2006.
- [24] D. Martin, C. Fowlkes, D. Tal, and J. Malik, “A database of human segmented natural images and its application to evaluating segmentation algorithms and measuring ecological statistics,” in *Proc. 8th Int’l Conf. Computer Vision*, vol. 2, July 2001, pp. 416–423.
- [25] P. Arbelaez, M. Maire, C. Fowlkes, and J. Malik, “Contour detection and hierarchical image segmentation,” *IEEE Trans. Pattern Anal. Mach. Intell.*, vol. 33, no. 5, pp. 898–916, May 2011.
- [26] C. Li, W. Yin, H. Jiang, and Y. Zhang, “An efficient augmented Lagrangian method with applications to total variation minimization,” *Computational Optimization and Applications*, vol. 56, no. 3, pp. 507–530, December 2013.
- [27] C. A. Metzler, A. Maleki, and R. G. Baraniuk, “From denoising to compressed sensing,” *IEEE Transactions on Information Theory*, vol. 62, no. 9, pp. 5117–5144, 2016.
- [28] C. A. Metzler, A. Mousavi, and R. G. Baraniuk, “Learned d-amp: Principled neural network based compressive image recovery,” in *Proceedings of the 31st International Conference on Neural Information Processing Systems*, ser. NIPS’17. Red Hook, NY, USA: Curran Associates Inc., 2017, p. 1770–1781.
- [29] W. Shi, F. Jiang, S. Liu, and D. Zhao, “Image compressed sensing using convolutional neural network,” *IEEE Transactions on Image Processing*, vol. 29, pp. 375–388, 2020.
- [30] D. Gilton, G. Ongie, and R. Willett, “Neumann networks for linear inverse problems in imaging,” *IEEE Transactions on Computational Imaging*, vol. 6, pp. 328–343, 2020.
- [31] W. Dong, P. Wang, W. Yin, G. Shi, F. Wu, and X. Lu, “Denoising prior driven deep neural network for image restoration,” *IEEE Transactions on Pattern Analysis and Machine Intelligence*, vol. 41, no. 10, pp. 2305–2318, 2019.

- [32] J. Zhang and B. Ghanem, “Ista-net: Interpretable optimization-inspired deep network for image compressive sensing,” in *2018 IEEE/CVF Conference on Computer Vision and Pattern Recognition*, 2018, pp. 1828–1837.